Available online at www.sciencedirect.com
ScienceDirect
Journal of Power Sources 178 (2008) 132–140
JOURNAL OF POWER SOURCES
www.elsevier.com/locate/jpowsour

Application of a thermally conductive pyrolytic graphite sheet to thermal management of a PEM fuel cell

Chih-Yung Wen [a,*], Guo-Wei Huang [b]

[a] *Department of Aeronautics and Astronautics, National Cheng-Kung University, No. 1, Ta-Shieh Road, Tainan 70101, Taiwan*
[b] *Department of Mechanical and Automation Engineering, Da-Yeh University, Chang-Hwa 51505, Taiwan*

Received 8 November 2007; received in revised form 10 December 2007; accepted 10 December 2007
Available online 23 December 2007

Abstract

This work experimentally investigates the thermal performance of a pyrolytic graphite sheet (PGS) in a single proton exchange membrane fuel cell (PEMFC). This PGS with high thermal conductivity serves as a heat spreader, reduces the volume and weight of cooling systems, and reduces and homogenizes the temperature in the reaction area of the fuel cells. A transparent PEMFC is constructed with PGS of thickness 0.1 mm cut into the shape of a flow channel and bound with the cathode gas channel plate. Eleven thermocouples are embedded at different positions on the cathode gas channel plate to measure the temperature distribution. The water and water flooding inside the cathode gas channels, with and without PGS, were successfully visualized. The locations of liquid water are correlated with the temperature measurement. PGS reduces the maximum cell temperature and improves cell performance at high cathode flow rates. The temperature distribution is also more uniform in the cell with PGS than in the one without PGS. Results of this study demonstrate the promising application of PGS to the thermal management of a fuel cell system.

Keywords: Proton exchange membrane fuel cell; Pyrolytic graphite sheet; Heat sink; Thermal management

1. Introduction

Many studies have, in recent years, revealed the promising applications of proton exchange membrane fuel cells (PEMFCs) in such areas as local power generation and zero-emission electric vehicles [1–3]. A typical hydrogen PEMFC can convert the chemical energy of reactants directly to electric energy with high efficiency and high environmental compatibility. A PEMFC has a working temperature from 60 to 100 °C and an efficiency of about 50%, such that the remaining 50% is waste heat. The waste heat must be discharged efficiently from the fuel cell to protect the proton exchange membrane. This issue of waste heat is even more important in a PEMFC stack system. Since the low PEMFC operating temperature limits the utilization of this waste heat, the main purpose of thermal management in a PEMFC is to ensure that a single cell or a stack operates within the specific range of temperatures.

The problem of thermal management in a PEMFC always accompanies that of water management and mass transport limitations. Since an understanding of the coupled fluid flow, heat and mass transfer processes within a single fuel cell and a fuel cell stack are of critical importance to the optimization of their designs, thermal and water management has been the subject of several fundamental experiment and theoretical studies [4–18]. Thermal management is well understood to remove waste heat properly to ensure that the PEMFC operates within a specific temperature range. An excessively high or low temperature on a membrane electrode assembly (MEA) surface may lead to membrane dehydration and water condensation (even flooding), respectively. The non-uniform temperature distribution over the MEA surface [13,16,18] may also reduce the reliability and durability of the MEA. Proper thermal management should prevent the formation of hot spots on MEA.

The waste heat may be discharged by convection, conduction, radiation or phase change. Cooling methods are decided mainly by the size of the fuel cell. Faghri and Guo [19] have summarized the commonly used cooling methods: (1) cooling with cathode oxidant flow; (2) cooling with separate air flow; (3) cooling with heat spreaders and (4) water cooling. Small PEMFC systems

* Corresponding author. Tel.: +886 6 2757575x63657; fax: +886 6 2349281.
E-mail address: cywen@mail.ncku.edu.tw (C.-Y. Wen).

0378-7753/$ – see front matter © 2007 Elsevier B.V. All rights reserved.
doi:10.1016/j.jpowsour.2007.12.040

do not usually incorporate separate cooling systems, because a forced air design with an external blower will extract 20–25% of the total power output in small fuel cell systems and the flow of cathode oxidant through the PEMFC systems also serves to carry away the heat generated by the reaction as it exits from the PEMFC [19]. For a larger PEMFC unit below 2 kW, air cooling serves to remove the waste heat. However, a separate reactant air supply and cooling system is needed to extract more heat from the stack. The cooling system will generally incorporate a blower and separate cooling channel plates through which air is blown. For PEMFC units between 2 and 10 kW, a careful decision must be made regarding whether air or water cooling should be used. For PEMFC units of over 10 kW, water cooling is required. A water cooling system will generally include separate cooling channel plates through which water passes, sensors to monitor the temperature and pressure of the cooling water, and an oil-free cooling water supplying pump. Special care must be taken to prevent the leakage of cooling water. For both air and water cooling systems, the separate cooling channel plates are spaced within the stack such that a temperature gradient across the bipolar plates can be minimized for heat transfer to occur. These cooling systems extract around 4–10% of the available electrical power of a PEMFC unit for pumping cooling water or blowing air through the stack to remove the waste heat. Currently, forced convection water or air flow is generally adopted as the cooling system. Nevertheless, it does not effectively homogenize the temperature inside a PEMFC, which homogenization is required to obtain high efficiencies. A cooling system with heat spreaders, which usually incorporates two-phase cooling devices like heat pipes [19–21], can be used to homogenize the temperature inside a PEMFC stack.

In a practical fuel cell power unit, the performance of the thermal management auxiliary system must be optimized to reduce the system weight and volume and the back work needed to run the system itself. This study focuses on these important issues of the thermal management of a PEMFC. A commercial pyrolytic graphite sheet (PGS) with high thermal conductivity is adopted as a heat spreader. PGS is used to transport heat out of the PEMFC through conduction, and then to dissipate this heat to surrounding air through natural convection. The constant voltage discharge performance of a transparent PEMFC that runs on dry hydrogen is compared with temperature measurements made using thermocouples during operation, and referenced to pictures taken with a digital video camera. The thermal performance of PGS in a PEMFC is evaluated.

PGS is a synthetically made material of a uniform form of highly oriented graphite polymer sheet. Table 1 shows the general characteristics of PGS [22]. PGS has a very high thermal conductivity of 600–800 W m^{-1} K, which is twice that of copper and 10 times that of ordinary graphite. PGS has a density of 1.0 g cm^{-3}, which is 1/9 that of copper and 1/3 that of aluminum. PGS is a flexible sheet and is easy to cut into any shape using simply a pair of hand-held scissors. PGS has high heat resistance and is stable up to about 500 °C. All these features of PGS make it a suitable material for providing thermal management and heat-sinking of a PEMFC system and reducing the volume and weight of cooling systems. It has been applied successfully in the thermal management of commercial portable electrical devices like laptop computers, where the spaces are limited.

Table 1
General characteristics of PGS [22]

Characteristics	Specifications
Thickness	0.10 ± 0.05 mm
Density	1 g cm^{-3}
Thermal conductivity	In-plane: 600–800 W m^{-1} K
	Normal to the sheet: approx. 15 W m^{-1} K
Electrical conductivity	10,000 S cm^{-1}
Tensile strength	19.6 MPa

2. Experimental

2.1. Design of transparent PEMFC with and without PGS

Fig. 1 schematically depicts the transparent fuel cell used in our research, which is similar to that designed by Tsai [23]. Two serpentine flow channel plates are placed between two thick transparent acrylic cover plates (10 cm × 10 cm) to visualize water formation at the channel/gas diffusion layer (GDL) interface. The serpentine channels on both anode and cathode sides (2 mm channel width, 2 mm rib width and 2 mm channel depth) were machined through stainless steel-316 plates to form an active cell area of 50 mm × 50 mm. The flow channel plates were coated with gold to reduce the ohmic resistance and increase corrosion protection. The membrane electrode assembly (MEA, a Nafion® 117 membrane with catalyst loading of anode and cathode: Pt/Ru 0.45 mg cm^{-2} and Pt 0.6 mg cm^{-2}) sandwiched in between two standard TORAY® carbon papers (TGP-H-090) as GDLs were placed in the middle of two flow channel plates. The PEMFC was clamped between two stainless end plates with four bolts that were tightened with a uniform torque of 10 N m.

Panasonic®'s PGS (EYGS182310) with a thickness of 0.1 mm was cut into the shape of the serpentine flow channels, as shown in Fig. 2, to evaluate the thermal performance of a PGS in the above transparent PEMFC. The trimmed PGS was placed

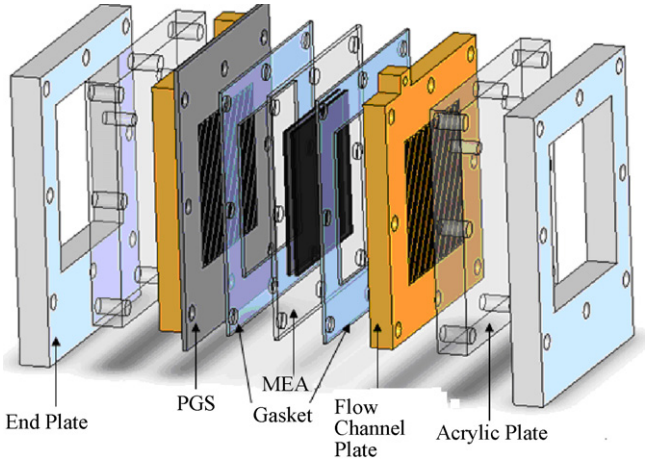

Fig. 1. Schematic of the transparent PEMFC.

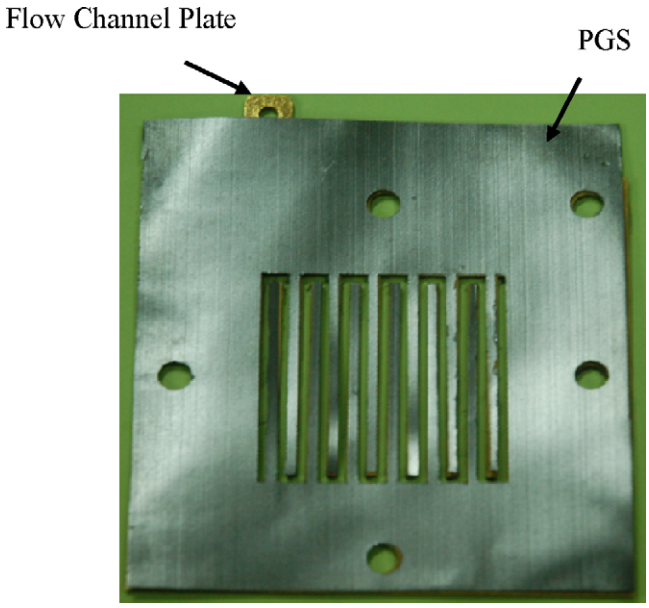

Fig. 2. Shaped PGS aligned with the flow channel plate on the cathode side.

between the cathode channel plate and GDL. The 1 cm × 10 cm extension to the area of flow channel plate on the PGS serves as a fin to reduce the cell temperature by free or forced air convection with the environment (Fig. 1). The simplicity of the hardware makes the PEMFC easily fabricated and assembled.

2.2. Experimental set-up

The experimental set-up, schematically depicted in Fig. 3, consists of a gas supply unit, a transparent PEMFC, a fuel cell test system, a digital video camera, 11 thermocouples, a thermocouple data log and a data acquisition system. The computer-controlled Arbin® fuel cell test system (Arbin Instruments, BT2000, 1 kW) composed of an electrical load and a gas handling system was used to control the load and anode and cathode gas parameters such as flow rate, dew point, and back-pressure. Since the minimum controllable flow rate for the gas handling system in the Arbin® fuel cell test system is 500 sccm, two needle-valves and two rotameters are placed between the gas bottles and the gas handling system (Fig. 3) yielding small flow rates for this small single cell (reaction area 5 cm × 5 cm). The flow of pure hydrogen and oxygen directly from gas bottles were regulated by needle-valves, with the mass flow controllers inside the gas handling system fully opened, before the gases were fed into the cell. The electrodes were purged with nitrogen between two experiments to realize reproducible initial conditions. The fuel cell was connected to the electrical load that was operated in constant voltage discharge mode. The current and voltage of the fuel cell under operation, gas flow parameters like volume flow rates, relative humidity and temperatures of the oxygen and hydrogen, and thermocouple readings are recorded using a data acquisition system. The digital video camera was used to visualize the water formation phenomena. Eleven T-type thermocouples protruded from the acrylic cover plate on the cathode side and their hot joints were in contact with the cathode channel plate yielding temperature distribution and an estimate of the average cell temperature of the PEMFC. The thermocouples were inserted very closely to the surface of the cathode gas channel plate adjacent to the GDL without penetrating it. The experimental set-up supports the simultaneous evaluation of cell performance and temperature and water distribution in a PEMFC under operation. Fig. 4 plots the 11 temperature points at which temperature is measured. They are points 1–6 from right to left along the horizontal line and points 5 and 7–11 from bottom to top along the vertical.

2.3. Experimental conditions

The experimental results presented in the next section were gained under the following conditions:

- The MEA underwent an activation process to ensure that the fuel cell has reached a stable status for every test. The process involved running the fuel cell at: (1) 0.6 V for 30 min; (2) 0.4 V for 30 min; (3) open-circuit potential for 1 min.

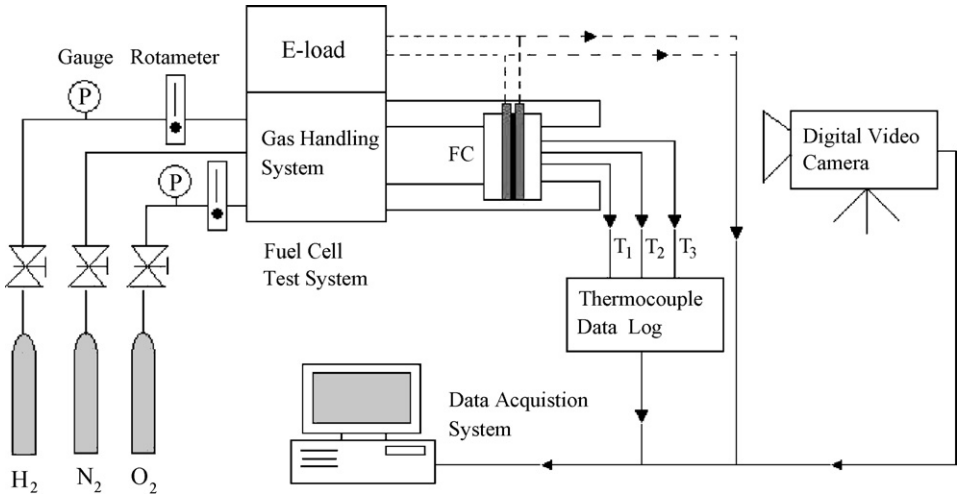

Fig. 3. Experimental set-up.

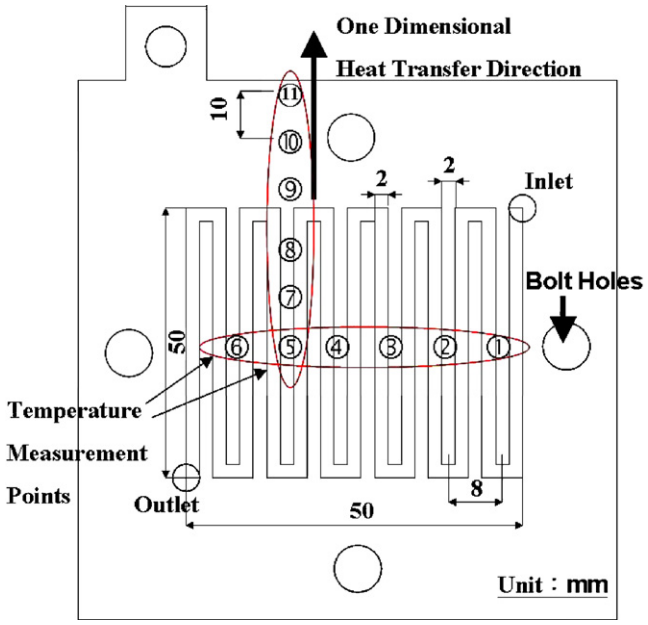

Fig. 4. The positions of the 11 temperature measurement points.

- The dry hydrogen (<10% RH) gas flow rate was 100 ml min^{-1}; the pressure was 3.72 atm and the temperature was 298 K.
- The oxygen was humidified to 80% RH at 50 °C.
- The oxygen flow rate was varied from 150 to 300 and 450 ml min^{-1}, at a pressure of 3.72 atm and a temperature of 298 K.
- The atmospheric temperature was 25 °C.

3. Results and discussion

3.1. Effect of PGS on cell performance

Fig. 5 plots the polarization curve that specifies the performance of the test cell throughout its operating range with and without PGS. The mass transport limitation shifts to higher current densities as the oxygen flow rate becomes smaller without PGS. The overall performance at an oxygen flow rate of 150 ml min^{-1} is generally higher than that at 450 ml min^{-1}.

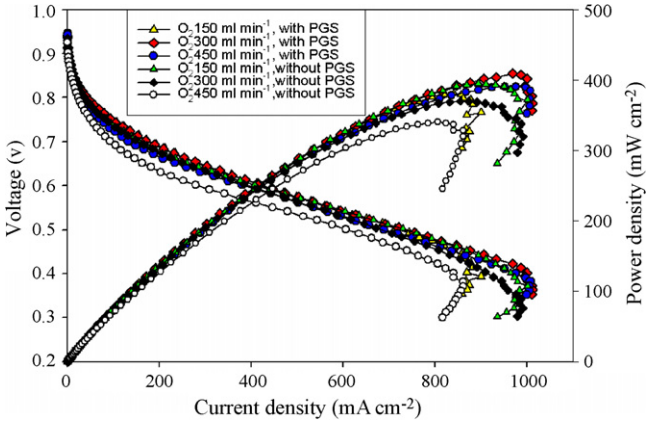

Fig. 5. Polarization curve of the test cell with and without PGS.

The power density at an oxygen flow rate of 150 ml min^{-1} is maximal at a current density of about 1000.0 mA cm^{-2}, which is significantly higher than the current density reached at an oxygen flow rate of 450 ml min^{-1}, because PEM requires water to have appropriate ionic conductivity. Without sufficient hydration, the membrane becomes too dry and the ohmic drop across the membrane is high. The transfer of water across a membrane proceeds by three mechanisms [24,25]: (1) electro-osmotic drag flux by hydrogen ion drag, (2) diffusion flux by water concentration gradient between anode and cathode and (3) convection flux by pressure gradient. In the experiments herein, hydrogen is fed dry to the anode. PEM hydration is achieved mainly by diffusion flux along the water concentration gradient between the anode and the cathode. A higher oxygen flow rate corresponds to the dragging of more water out of the cell and the diffusion of less water back to the anode, such that power density declines as the oxygen flow rate increases.

The attachment of PGS to the test cell changes its performance. The mass transport limitation shifts to higher current densities as the oxygen flow rate becomes larger. The overall performance of the cell at an oxygen flow rate of 300 ml min^{-1} is very close to that at 450 ml min^{-1}. The power density for the oxygen flow rate at 450 ml min^{-1} is maximal at a current density of about 1000.0 mA cm^{-2}, which is higher than the current density reached at an oxygen flow rate of 150 ml min^{-1}, because PGS reduces the average temperature of the cell and causes more water condensation than without PGS. Increasing the oxygen flow rates removes more water and alleviates the problem of flooding. The use of PGS is advantageous under relatively dry conditions and high flow rates. The coupled fluid flow, heat and mass transfer proceed within the test cell with and without PGS, as will be explained in Section 3.2 based on flow visualization and temperature measurements.

The overall performance of the test cell at oxygen flow rates of 300 and 450 ml min^{-1} with PGS is better than that without PGS; the reverse is true at an oxygen flow rate of 150 ml min^{-1}.

3.2. Effect of PGS on temperature and distribution of liquid water

Fig. 6 presents experimental images of the cathode flow field and the measured temperatures of the test cell without PGS. The cell was operated in a constant voltage discharge mode (0.4 V) at different oxygen flow rates. This operation voltage is very close to the mass transport limitation. The inlet is in the upper right corner and the outlet is in the lower left corner, as revealed by red tubes in the photographs. Each photograph was captured at 6 min after current loading, when the "partial flooding" of the cathode catalyst layer, as described by Tüber et al. [12], occurred. At a flow rate of 150 ml min^{-1} (with corresponding current density of 0.964 A cm^{-2}), water vapor condenses at the cover plate in the form of very small droplets and appears before the middle section of the serpentine flow channel (grey area in the photo). At 300 ml min^{-1} (with corresponding current density of 0.909 A cm^{-2}), water droplets appear mainly beyond the

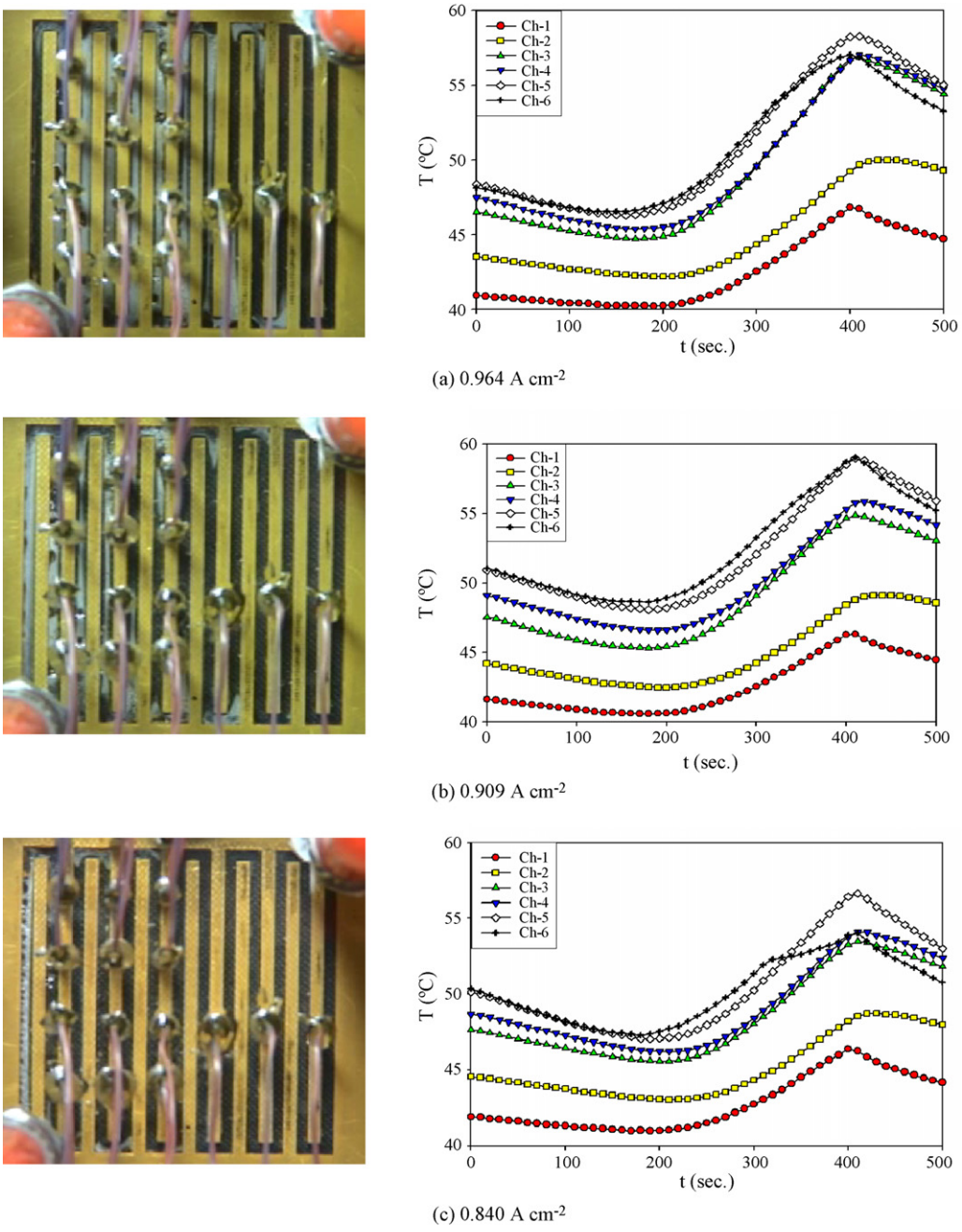

Fig. 6. Images of cathode gas flow channels and temperature measurement without PGS for oxygen flow rates of: (a) 150 ml min^{-1}; (b) 300 ml min^{-1} and (c) 450 ml min^{-1}. (For interpretation of the references to color in text, the reader is referred to the web version of the article.).

middle section of the serpentine flow channel. At 450 ml min^{-1} (with a corresponding current density of 0.840 A cm^{-2}), water droplets appear only at the later corners and the last section of the serpentine flow channel. The higher water activity and membrane hydration at a lower flow rate make the current density higher. The flow visualization clearly demonstrates the better performance of the polarization curve at an oxygen flow rate of 150 ml min^{-1} than at 300 ml min^{-1} or 450 ml min^{-1}, described earlier. Visible water drops are observed in the channel beyond measurement point 5 in all three cases, indicating that water flooding is more serious in the later section of the serpentine channel.

The thermocouple measurements at points 1–6 yield corresponding temperature distributions in the test. The temperatures were measured after current loading. The activation process described in Section 2.3 yielded the initial temperature distribution (at time zero). The early decline in each temperature was caused by convective heat transfer by the cathode flow. After around 200 s, the heat generation started to dominate and the temperature rose accordingly. The load was disconnected after 400 s and the temperatures in the cell fell again. As seen, the downstream temperatures are generally higher than the upstream temperatures in all three cases. In the experiments, since dry hydrogen was supplied, all of the water needed in the membrane

came from the cathode gas flow, including the water produced by the electrochemical reactions. As a result, both the membrane hydration and the water activity increased along the flow path. The temperature at point 6 fell to less than that at point 5 at a later time in each case because of the water flooding in the serpentine channel downstream of point 5, as described earlier. The local water flooding of the cathode worsens local performance. The temperature measurements are consistent with the flow visualization and polarization curve.

Fig. 7 presents the experimental images of the cathode flow field and the measured temperatures of the test cell with PGS. Like without PGS, the cell was operated in a constant voltage discharge mode (0.4 V) at different oxygen flow rates and the images were captured at 6 min after current loading. The inlet and outlet appear as red tubes in the photographs in the upper right-hand corner and the lower left-hand corner, respectively. At 150 ml min^{-1} (with a corresponding current density of 0.900 A cm^{-2}), water vapor, in the form of small condensing droplets at the cover plate, appears at the beginning of the serpentine flow channel. A comparison with Fig. 6(a) demonstrates that the water vapor is much denser than in the case without PGS and the small droplets are larger. Water drops can also be seen at the second channel and a few other locations downstream. The water flooding of the cathode causes the performance loss and reduces the mass transport limitation, as shown in Fig. 5. At 300 ml min^{-1} (Fig. 7(b), with a corresponding current den-

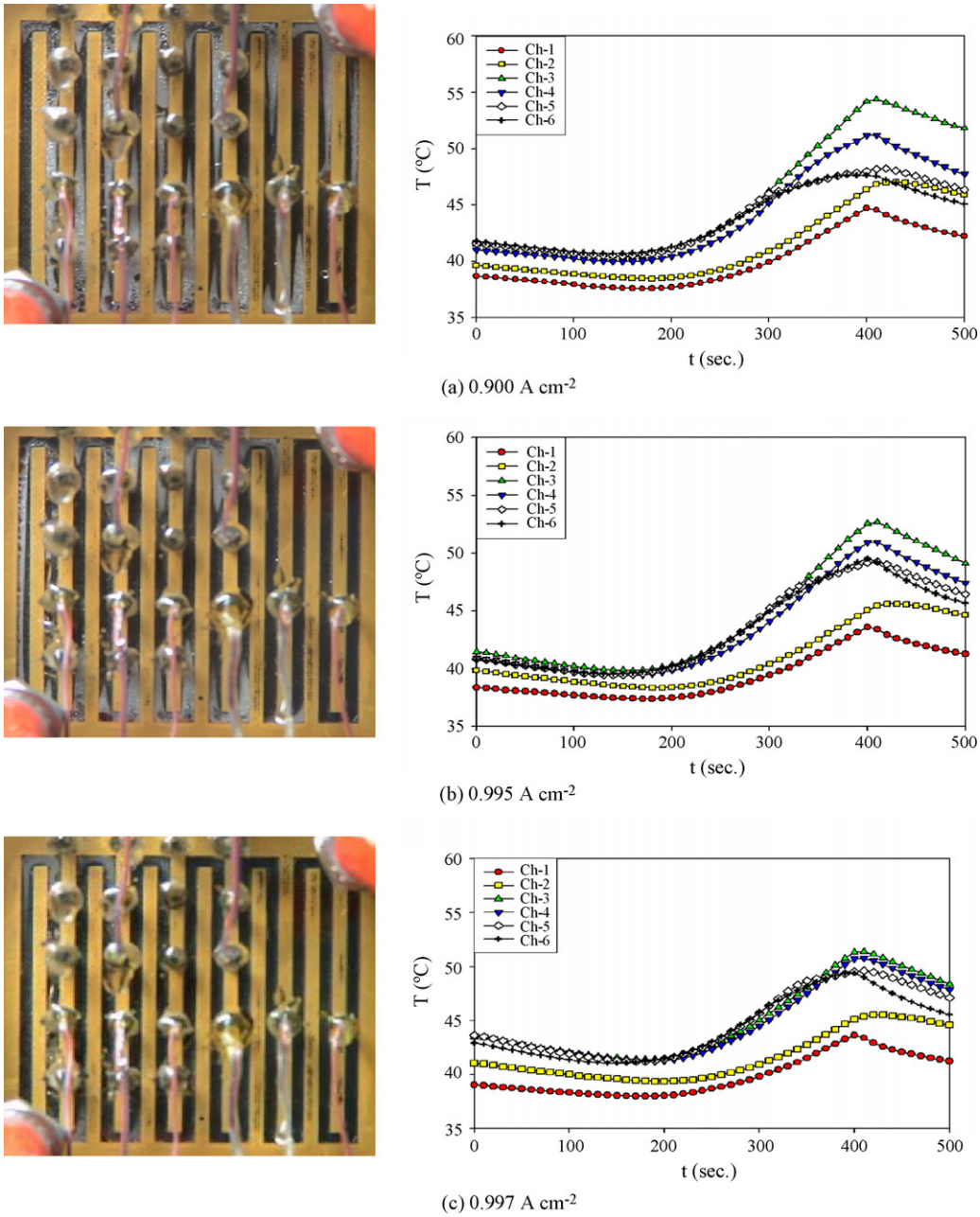

Fig. 7. Images of cathode gas flow channels and temperature measurement with PGS for oxygen flow rates of: (a) 150 ml min^{-1}; (b) 300 ml min^{-1} and (c) 450 ml min^{-1}. (For interpretation of the references to color in text, the reader is referred to the web version of the article.).

sity of 0.995 A cm^{-2}), water droplets appear later than the case with 150 ml min^{-1}. The water droplets are observed before the middle section of the serpentine flow channel. At 450 ml min^{-1} (Fig. 7(c), with a corresponding current density of 0.97 A cm^{-2}), water droplets appear only at the later corners and the last section of the serpentine flow channel. Increasing the oxygen flow rate removes more water and alleviate the problem of flooding. The flow visualization in Fig. 5 clearly reveals the better polarization curve performance at an oxygen flow rate of 450 ml min^{-1} than at 150 ml min^{-1}, as described earlier. The results of the flow visualization are consistent with the polarization curve performance. As in the case without PGS, visible water drops are observed in the later section of the serpentine channel at all three oxygen flow rates, indicating serious water flooding.

The corresponding temperature distributions in the test cell with PGS, shown in Fig. 7, are much more uniform than in the case without PGS. The difference between the maximum and minimum temperatures is lower. In the early stage, the initial temperatures at measurement points 3–6 are very close for all three oxygen flow rates. PGS acts as an effective heat spreader. The decline of temperatures at points 5 and 6 at late times in Fig. 7 for each oxygen flow rate is caused by the water flooding observed in the downstream serpentine channel, described earlier. The local water flooding of the cathode yields the local performance loss. The results of the temperature measurement are again consistent with the flow visualization.

Fig. 8 plots the typical variations of maximum, minimum and average temperatures taken from the data between 200 and 400 s for 300 ml min^{-1} in Figs. 6 and 7. As seen clearly, PGS reduces and homogenizes the temperature inside the PEMFC. The maximum, minimum and average temperatures in the PEMFC with PGS are as much as 8, 3 and 6 °C lower, respectively, comparing with that without PGS. The difference between the maximum and minimum temperatures also is lower. The lower temperature inside PEMFC with PGS makes water condensation easier than in the case without PGS, especially at a low oxygen flow rate.

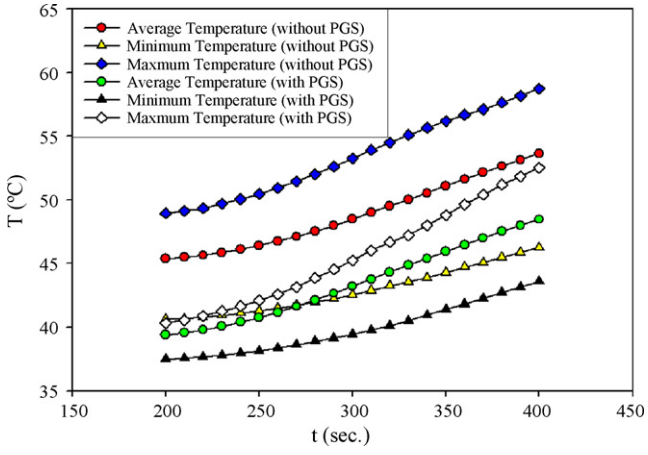

Fig. 8. Effect of PGS on temperature of the cell in the constant voltage mode of 0.4 V discharge mode.

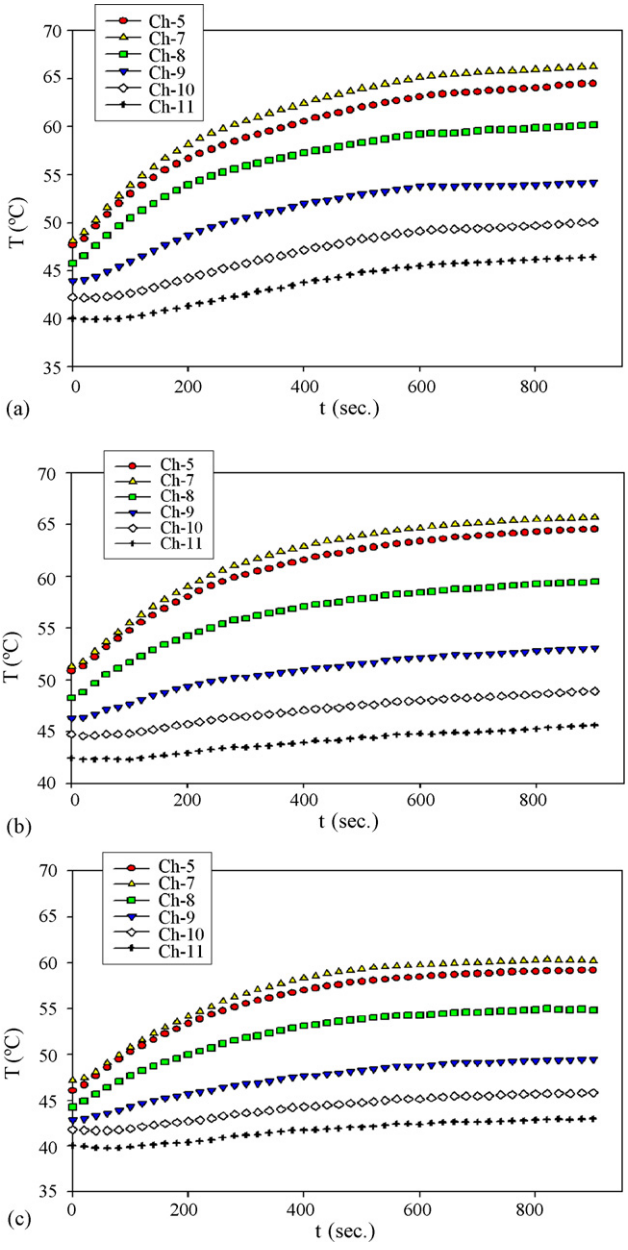

Fig. 9. Temperature variations of measurement points 5 and 7–11 without PGS. The cell is operated in the constant voltage mode of 0.5 V with oxygen flow rates of: (a) 150 ml min^{-1}; (b) 300 ml min^{-1} and (c) 450 ml min^{-1}.

3.3. Effect of PGS on heat transfer

The heat transfer rates were estimated by making thermocouple measurements at points 5 and 7–11 in the vertical direction to demonstrate the heat transfer capability of PGS (Fig. 4). The temperature measurement in Figs. 6 and 7 indicates the temperatures are maximal near point 5 in both cases, with and without PGS, before water flooding occurs. These experiments were designed such that the cell was operated in a constant voltage discharge mode at 0.5 V with different oxygen flow rates to avoid the flooding problem and to estimate the heat transfer rates near the hot spot. Figs. 9 and 10 plot the increase in temperature with time, without and with PGS, respectively.

Table 2
Estimated heat transfer rates for cells with and without PGS at three oxygen flow rates

	Oxygen flow rate (ml min^{-1})	Ch 9 (°C)	Ch 10 (°C)	Ch 11 (°C)	Q (W)
Without PGS	150	54.0	49.7	46.2	0.023
	300	52.8	48.7	45.3	0.022
	450	49.3	45.7	42.8	0.021
With PGS	150	49.4	44.2	41.3	0.082
	300	48.1	43.1	39.9	0.079
	450	46.9	41.6	38.9	0.075

The measurements were made for 900 s when all temperatures reached quasi-steady values. The zero time was when the heat generation inside the PEMFC started to dominate the convective heat extracted by cathode flow, resulting in an increase in temperature, as described earlier. As seen in Fig. 4, the measurement points 5, 7 and 8 are inside the reaction area where heat is generated, while points 9–11 are outside the reaction area. The temperature at point 7 is a little higher than that at point 5 in Fig. 9 for the cell without PGS at all three flow rates. However, in Fig. 10 for the cell with PGS, the temperatures at points 5 and 7 are almost identical. The temperature at point 8 near the edge of the reaction area is lower than those at points 5 and 7 for cells with and without PGS. The temperature decreases almost linearly from points 9–11 in Figs. 9 and 10. Hence, one-dimensional Fourier's law is used to estimate the heat transfer rates, $\dot{Q}$:

$$\dot{Q} = -k_{ss} A_{ss} \frac{dT}{dy}, \tag{1}$$

for the cell without PGS, and

$$\dot{Q} = -k_{ss} A_{ss} \frac{dT}{dy} - k_{PGS} A_{PGS} \frac{dT}{dy}, \tag{2}$$

for the cell with PGS. Here k is the thermal conductivity and A is the cross-sectional area. The subscripts ss and PGS denote the materials, stainless steel and PGS, respectively. Table 2 shows the estimated heat transfer rates for cells with and without PGS at three oxygen flow rates, where k_{ss} and k_{PGS} are taken to be 14.9 and 700 W m^{-1} K, respectively, $A_{ss} = 2\,\text{mm} \times 2\,\text{mm} = 4 \times 10^{-6}\,\text{m}^2$, and $A_{PGS} = 2\,\text{mm} \times 0.1\,\text{mm} = 2 \times 10^{-7}\,\text{m}^2$. Table 2 presents the quasi-steady temperatures of points 9–11, taken from Figs. 9 and 10; they are fitted with a straight line. The temperature gradient in Eqs. (1) or (2) is estimated from the slope of this straight line. As seen in Table 2, PGS effectively lowers the temperature and increases the heat transfer rate. When PGS is attached, the heat transfer rate is increased by a factor of approximately four.

In the experiments herein, PGS is utilized to transport heat out of the PEMFC through conduction, and then to dissipate the heat to surrounding air through the extended fin area by natural convection. The hot spot (local higher temperature region) over the whole surface of the MEA can be estimated from the temperature measurements. Knowing the position of the hot spot helps in designing the geometry of PGS. The idea that underlies future application is to introduce PGS to positions where the heat generation is high in a PEMFC stack to provide effective cooling and create a more uniform stack temperature.

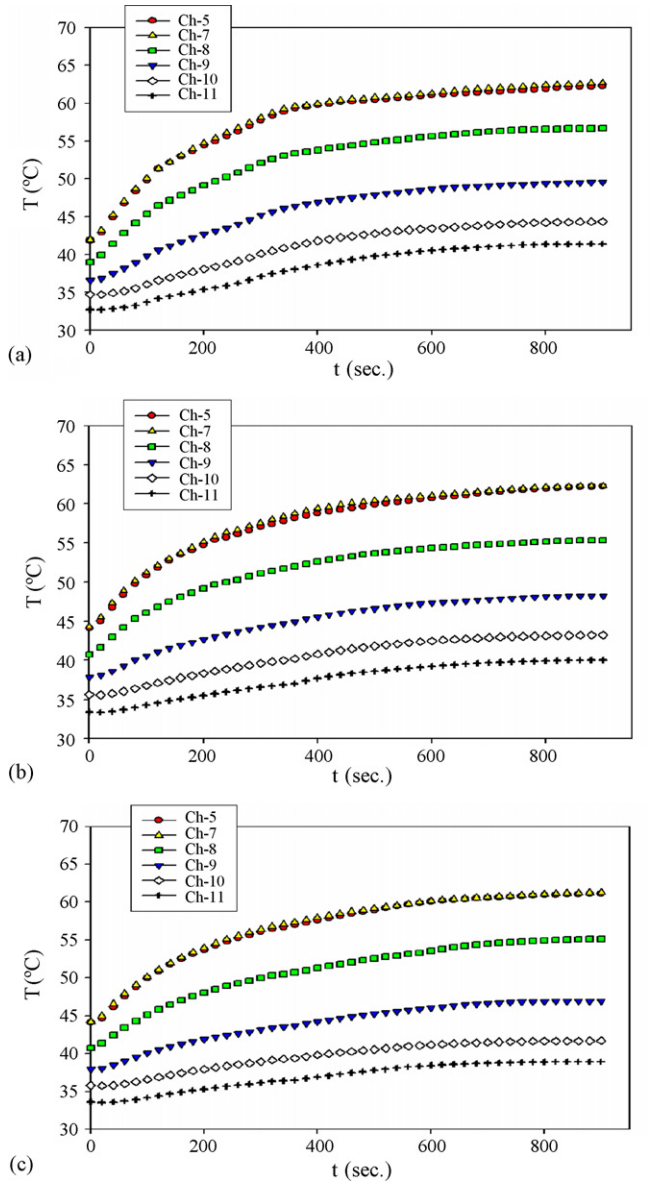

Fig. 10. Temperature variations of measurement points 5 and 7–11 with PGS. The cell is operated in the constant voltage mode of 0.5 V with oxygen flow rates of: (a) 150 ml min^{-1}; (b) 300 ml min^{-1} and (c) 450 ml min^{-1}.

4. Conclusions

This work presents a novel approach of PEMFC cooling, in which most of the waste heat is transferred by thermal conduction via PGS and then discharged to ambiance. Accordingly, the system can be miniaturized and weight, volume and costs kept to a minimum by reducing the number of ancillary components. Images of a transparent cathode flow channel were obtained and temperature measurements made under different operating conditions to understand the effects of PGS on cell performance. PGS effectively lowers the temperatures inside the cell and increases the heat transfer rate. Results of this study demonstrate that PGS provides an innovative, feasible and economic means of thermally managing a fuel cell system. An experimental investigation of the effects of the PGS on the performance and thermal management of a PEMFC stack is ongoing and will be reported upon in the future.

Acknowledgements

The authors would like to thank the National Science Council of the Republic of China, Taiwan, for financially supporting this research under Contract No. NSC-94-2212-E-212-012.

References

[1] P. Costamagna, S. Srinivasa, J. Power Sources 102 (2001) 253–269.
[2] M.H. Fronk, D.L. Wetter, D.A. Masten, A. Bosco, SAE pap. 1 (2000) 373–390.
[3] X. Yu, B. Zhou, CSME Forum S7 (2004) 1091–1100.
[4] T.F. Fuller, J. Newman, J. Electrochem. Soc. 139 (5) (1992) 1332–1337.
[5] T.V. Nguyen, R.E. White, J. Electrochem. Soc. 140 (8) (1993) 2178–2186.
[6] T.F. Fuller, J. Newman, J. Electrochem. Soc. 140 (5) (1993) 1218–1225.
[7] R. Mosdale, S. Srinivasan, Electrochim. Acta 40 (4) (1995) 413–421.
[8] J. Musser, C.Y. Wang, Proceedings of NHTC'00, Pittsburgh, PA, August 2000, NHTC2000-12151.
[9] R. Andrew, X.G. Li, J. Power Sources 102 (2001) 82–96.
[10] Y.J. Zhang, M.G. Ouyang, J.X. Luo, Z. Zhang, Y.J. Wang, SAE pap. 1 (2003) 11–46.
[11] R. Hahn, M. Krumm, H. Reichl, Proceedings of 19th IEEE SEMI-THERM Symposium, San Jose, CA, March 2003, pp. 202–209.
[12] K. Tüber, D. Pócza, C. Hebling, J. Power Sources 124 (2003) 403–414.
[13] A. Hakenjos, H. Muenter, U. Wittstadt, C. Hebling, J. Power Sources 131 (2004) 213–216.
[14] W.M. Yan, F. Chen, H.Y. Wu, C.Y. Soong, H.S. Chu, J. Power Sources 129 (2004) 127–137.
[15] X. Yu, B. Zhou, A. Sobiesiak, J. Power Sources 147 (2005) 184–195.
[16] H. Ju, H. Meng, C.Y. Wang, Int. J. Heat Mass Transf. 48 (2005) 1303–1315.
[17] L. Dumercy, R. Glises, H. Louahlia-Gualous, J.M. Kauffmann, J. Power Sources 156 (2006) 78–84.
[18] M. Wang, H. Guo, C. Ma, J. Power Sources 157 (2006) 181–187.
[19] A. Faghri, Z. Guo, Int. J. Heat Mass Transf. 48 (2005) 3891–3920.
[20] Z. Guo, A. Faghri, J. Power Sources 167 (2007) 378–390.
[21] R. Rullière, F. Lefèvre, M. Lallemand, J. Heat Mass Transf. 50 (2007) 1255–1262.
[22] http://panasonic. com/industrial/components/thermal/thm_hsm.htm, September 2007.
[23] B.T. Tsai, Visualization of water formation in the PEMFC and the effects of interfacial pressure on its performance, Master Thesis, Da-Yeh University, Taiwan, 2005.
[24] J.S. Yi, T.V. Nguyen, J. Electrochem. Soc. 145 (1998) 1149–1159.
[25] S.H. Ge, B.L. Yi, J. Power Sources 124 (2003) 1–11.